Magnetic Resonance Imaging 60 (2019) 20–31

Contents lists available at ScienceDirect

Magnetic Resonance Imaging

journal homepage: www.elsevier.com/locate/mri

Original contribution

A two-step low rank matrices approach for constrained MR image reconstruction

Shuli Ma, Huiqian Du*, Wenbo Mei

School of Information and Electronics, Beijing Institute of Technology, Beijing 100081, China

ARTICLE INFO

Keywords:
MRI
Annihilating filter
Low rank matrix
Difference images
ADMM

ABSTRACT

Low-rank structure is a powerful priori characteristic that is exploited in constrained magnetic resonance imaging (MRI). In this paper, we build two low rank matrices T_V and T_H from weighted *k*-space data according to the duality between the sparsity in the difference image and the low-rankness of a reciprocal spectral domain. Then, we propose a two-step constrained MR image reconstruction method. First, the vertical and horizontal difference images are recovered via enforcing low-rankness of matrices T_V and T_H. Then, the image is reconstructed via the least squares method. In the first step, the nuclear norm of a matrix is replaced by the minimum Frobenius norm of two factorization matrices and the alternating direction method of multipliers (ADMM) algorithm is applied to recover the difference images. This singular value decomposition (SVD) free method leads to fast reconstruction. The experimental results demonstrate that the proposed method outperforms other low rank based methods.

1. Introduction

Magnetic resonance imaging (MRI) is a widely used imaging modality for clinical diagnosis because of its non-invasiveness and the ability to effectively depict soft tissue changes. However, the inherently slow scanning time limits its applications. To address this issue, many sparse sampling methods have been proposed to accelerate MRI [1–6]. The crux of these methods is to exploit the features of images to compensate for incomplete measurements. For example, compressed sensing based MRI methods have successfully exploited the sparsity of magnetic resonance images in various transform domains, such as wavelet transform [7], contourlet transform [8], and gradient transform [9–12].

Low-rank structure is another useful feature for sparse sampling [13–16]. In 2009, Candes et al. [15–16] proposed low-rank matrix completion from randomly located observations by minimizing the nuclear norm of the matrix. Inspired by the matrix completion method, Chen and Chi [13] proposed recovering a 2D signal $X \in \mathbb{R}^{n_1 \times n_2}$ with spectral sparsity r from at least $\mathcal{O}(r\ log^4(n_1 n_2))$ time-domain samples. They constructed a two-fold Hankel matrix X_e called the effective enhanced form of X, and reconstructed X by minimizing the nuclear norm of X_e.The MR image reconstruction problem in the sparse sampling scenario can be seen as a *k*-space matrix completion problem. In 2015, Kong and Ye [17] proposed constructing a low-rank 2D-Hankel matrix H formed by *k*-space data. The idea originates from the fact that the sparsity of an MR image leads to the low-rankness of a matrix in the reciprocal spectral domain due to the annihilating filter relationship [14,17–19]. They estimated the fully sampled *k*-space data by enhancing the low rankness of matrix H. According to the theoretical guarantee proposed in [13,15–16], the sparser the MR image is, the smaller the rank of matrix H is, and the fewer measurements are needed for recovering *k*-space data. Haldar developed a low rank model named LORAKS for the reconstruction of an MR image with limited support or an MR image that has a smooth phase [20]. He constructed low rank matrices named C, G and S using local *k*-space neighbourhood data, and applied an iterative majorize-minimize (MM)-based algorithm to reconstruct images [20–23]. Matrix C has a structure similar to that proposed by Kong and Ye [17]. The same conclusion exists for matrix S, and the results showen in [20] demonstrated that enforcing the low-rankness of matrix S leads to better reconstruction than enforcing the low-rankness of matrix C.

In this paper, we propose a two-step image reconstruction scheme. In the first step, we construct two low rank matrices T_V and T_H with weighted *k*-space data and recover the vertical difference image X_V and the horizontal difference image X_H by enforcing the low rankness of T_V and T_H. In the second step, the image X is estimated from X_V and X_H using the least squares method. To reduce the computational complexity, we replace the nuclear norm of the low-rank matrix with the

* Corresponding author.
E-mail addresses: duhuiqian@bit.edu.cn (H. Du), wbmei@bit.edu.cn (W. Mei).

https://doi.org/10.1016/j.mri.2019.03.019
Received 25 September 2018; Received in revised form 20 March 2019; Accepted 23 March 2019

minimum Frobenius norm of two factorization matrices, which can reduce the computational time due to the absence singular value decomposition (SVD). In addition, the alternating direction method of multipliers (ADMM) algorithm is applied to solve the corresponding optimization problem. In [24], Patel et al. proposed reoncstruct X_V and X_H first, and then reconstruct the image X. In constrast, we reconstruct the difference images X_V and X_H by enhancing the low-rankness of the matrices T_V and T_H instead of enhancing the sparsity of X_V and X_H. Experimental results show that the proposed method outperforms the LORAKS method and the gradient sparsity based method [24], which demonstrate the effectiveness of our method.

The rest of the paper is organized as follows. Section 2 explains the proposed method. The results and analysis are presented in Section 3, the conclusions are presented in Section 4.

2. Method

As indicated in previous research works, a lower rank matrix needs a smaller amount of measurements to be recovered. Given the duality between the sparsity in the primary space and the low-rankness of a matrix in the spectral domain, we hope to find a sparser representation of the image so that we can construct a lower rank matrix in the spectral domain.

Generally, the horizontal and vertical differences of an MR image are sparser or more compressible than the original image, as shown in Fig. 1. If the image is a piecewise constant image, its vertical and horizontal difference images would only contain nonzero values around the edges where the dayta are sparse. Therefore, we chose to construct low-rank matrices with weighted k-space measurements and reconstruct sparse vertical and horizontal difference images by enhancing the low rankness of these matrices and then estimating the original MR image.

In this section, the idea behind the LORAKS method will be introduced to reconstruct the difference images. We construct two types of low-rank matrices: C_V and C_H matrices, S_V and S_H matrices. For the sake of convenience, we use T_V to represent C_V or S_V, and T_H represent C_H or S_H. Next, we begin by demonstrating how to construct T_V and T_H using the weighted k-space data according to the annihilating filter and the properties of the 2D Fourier transform. Then, a two-step reconstruction method is described in detail.

2.1. Low rank matrices T_V and T_H

Recently, researchers have proposed constructing low rank Toeplitz-like or Hankel-like structural matrices using spectral data under the assumption that the image is sparse or limited in support. Let $X \in \mathbb{C}^{m\times n}$ denote an MR image. If X is sparse or limited in support, it is easy to find a smooth function or an annihilating function $A \in \mathbb{C}^{m\times n}$ that does not overlap with the support of X, i.e., Ω_X:

$$X(i,\ j)A(i,\ j) = 0,\quad \text{where } A(i,j) = 0\ ,\ \forall\ (i,j)\ \in\ \Omega_X \tag{1}$$

where $(i,\ j)$ denotes the element position of X, $i = 1,\ 2,\ \dots\ ,\ m$, and $j = 1,\ 2,\ \dots\ ,\ n$. Let $\mathscr{X}$ and $\mathscr{A}$ denote the Fourier transform of X and A respectively. The filter $\mathscr{A}$ can be accurately truncated by a circular window with the radius R. According to the 2D convolution theorem, the following relationship is implied:

$$\sum_{(p_k,q_k)\in\Lambda_R} \mathscr{X}\ [w - p_k, u - q_k]\ \mathscr{A}\ [p_k, q_k]\ \approx\ 0 \tag{2}$$

where $\Lambda_R = \{(p_k,\ q_k)\ \in\ \mathbb{Z}^2 :\ {p_k}^2 + {q_k}^2\ \le\ R^2\}$ and (w,u) belong to the set of 2-D frequencies defined by $\Omega_{(w,u)} = \{(w_{k_1}, u_{k_2}) : k_1 \in \{1,\cdots,m\}, k_2 \in \{1,\cdots,n\}, \forall (w,u) \in \mathbb{Z}^2\}$. Assume that the elements in Λ_R have been assigned an order such that the point $(p_k,\ q_k)$ corresponds to the k^{th} element of Λ_R, and $k\ =\ 1,\ \dots\ ,\ N_R$, where N_R is the number of elements in Λ_R. If we introduce a vector $\overline{\mathscr{A}}$ to denote the vectorized annihilating filter $\mathscr{A}$ in Λ_R, then Eq. (2) can be reformulated as a matrix-vector product:

$$C\ \overline{\mathscr{A}}\ \approx\ 0 \tag{3}$$

where $C \in\ \mathbb{C}^{L\times N_R}$ is the chopped convolution matrix composed of $\mathscr{X}$, i.e. $C\ (l,\ k) = \mathscr{X}\ [w_l - p_k,\ u_l - q_k]$, $L\ =\ (m - 2R + 1)(n - 2R + 1)$, $l\ =\ 1,\ \dots\ ,\ L$, where $\mathscr{X}\ (w_l,\ u_l)$ is the l^{th} element of $\mathscr{X}$, and $(p_k,\ q_k)$ denotes the k^{th} element of $\overline{\mathscr{A}}$. From Eq. (3), we can see that matrix C is rank deficient.

In LORAKS method, Haldar proposed to construct low rank matrices exploiting the sparsity or the smooth phase of the image. Generally, the differences images are sparser than the original image, as shown in Fig. 1. Thus, we introduce the idea behind the LORAKS method into the gradient domain. We construct two low-rank matrices T_V and T_H with weighted k-space data. The difference images X_V and X_H are obtained using the following equations:

$$X_V(i,\ j)\ =\ X(i,\ j)\ -\ X(i-1,\ j), \tag{4}$$

$$X_H(i,\ j)\ =\ X(i,\ j)\ -\ X(i,\ j-1) \tag{5}$$

Smooth functions A_V and A_H that satisfy the following annihilating filter relationship can be easily found.

$$X_V(i,\ j)A_V(i,\ j)\ =\ 0,\ \text{ where } A_V(i,\ j)\ =\ 0\ ,\quad \forall\ (i,\ j)\ \in\ \Omega_{X_V} \tag{6}$$

$$X_H(i,\ j)A_H(i,\ j)\ =\ 0,\ \text{ where } A_H(i,\ j)\ =\ 0\ ,\quad \forall\ (i,\ j)\ \in\ \Omega_{X_H} \tag{7}$$

where Ω_{X_V} and Ω_{X_H} are the supports of X_V and X_H respectively.

We use $\mathscr{X}_V$ and $\mathscr{X}_H$ to denote the Fourier transform of difference images which can be obtained from k-space data by Eqs. (8) and (9), respectively, as follows.

$$\mathscr{X}_V(w,\ u)\ =\ (1\ -\ e^{-2\pi \mathrm{j}w/m}\ )\mathscr{X}(w,\ u) \tag{8}$$

$$\mathscr{X}_H(w,\ u)\ =\ (1\ -\ e^{-2\pi \mathrm{j}u/n}\ )\mathscr{X}(w,\ u) \tag{9}$$

We also call $\mathscr{X}_V$ and $\mathscr{X}_H$ the weighted k-space data in this paper. According to

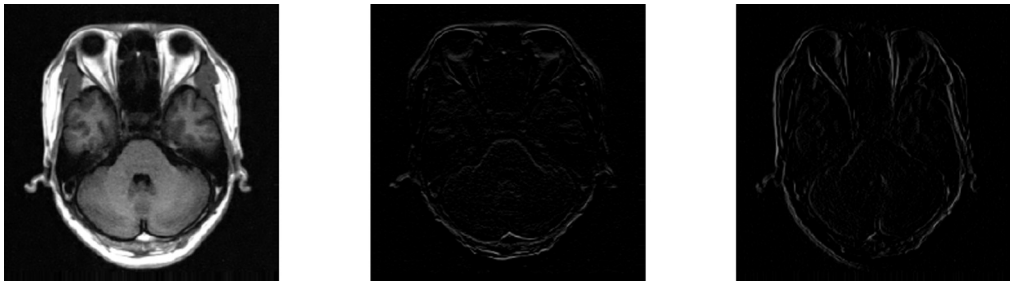

(a) Original MR image (b) Vertical difference image (c) Horizontal difference image

Fig. 1. (a)–(c) MR image that is 256 × 256 and its differences.

$$\sum_{(p_k,q_k)\in\Lambda_R} \mathscr{X}_V\,[w-p_k, u-q_k]\;\mathscr{A}_V\,[p_k,q_k] \;\approx\; 0 \tag{10}$$

$$\sum_{(p_k,q_k)\in\Lambda_R} \mathscr{X}_H\,[w-p_k, u-q_k]\;\mathscr{A}_H\,[p_k,q_k] \;\approx\; 0 \tag{11}$$

where $\mathscr{A}_V$ and $\mathscr{A}_H$ are the truncated Fourier transform of the smooth functions A_V and A_H respectively, we can obtain two chopped low rank convolution matrices $C_V \in \mathbb{C}^{L\times N_R}$ and $C_H \in \mathbb{C}^{L\times N_R}$ composed of the entries in $\mathscr{X}_V$ and $\mathscr{X}_H$, respectively. That is, $C_V(l,\ k) = \mathscr{X}_V\ [w_l - p_k,\ u_l - q_k]$, and $C_H(l,\ k) = \mathscr{X}_H\ [w_l - p_k,\ u_l - q_k]$.

In [14,17,25], the authors state that for a 1D signal with sparsity r, the rank of the corresponding Hankel structure matrix is r. They also give the proof and extend this principle to 2D images, i.e., r *sparse image* $\overset{F}{\rightleftarrows}$ r *rank* $2-D$ *Hankel structure matrix*. Therefore, we know that $rank(C_V) < rank(C)$, and $rank(C_H) < rank(C)$.

As in LORAKS we construct another type of low-rank matrices, namely, S_V and S_H. From Eqs. (6) and (7), we know that

$$X_V(i,\ j)A_V(i,\ j) \;=\; X_V^*(i,\ j)A_V^*(i,\ j) \tag{12}$$

$$X_H(i,\ j)A_H(i,\ j) \;=\; X_H^*(i,\ j)A_H^*(i,\ j) \tag{13}$$

where $*$ denotes the complex conjugation.

Based on the convolution theorem, we have:

$$X_V(i,\ j)A_V(i,\ j) \;\Leftrightarrow\; \sum_{(p_k,q_k)\in\Lambda_R} \mathscr{X}_V\,[w-p_k,\ u-q_k]\,\mathscr{A}_V\,[p_k,\ q_k]$$

According to the complex conjugation property of the Fourier transform, i.e., if $f(x)\Leftrightarrow F(w)$, then $f^*(x)\Leftrightarrow F^*(-w)$, and we have:

$$X_V^*(i,\ j)A_V^*(i,\ j) \Leftrightarrow \sum_{(p_k,q_k)\in\Lambda_R} X_V^*[-w+p_k,\ -u+q_k]A_V^*[-p_k,\ -q_k]$$

Since the index of $(p_k,\ q_k)$ is symmetrical and $(-p_k, -q_k)\in\Lambda_R$, then

$$\sum_{(p_k,q_k)\in\Lambda_R} \mathscr{X}_V^*[-w+p_k,\ -u+q_k]\,\mathscr{A}_V^*[-p_k,\ -q_k] = \sum_{(p_k,q_k)\in\Lambda_R} \mathscr{X}_V^*[-w-p_k,\ -u-q_k]\,\mathscr{A}_V^*[p_k,\ q_k]$$

Therefore, Eqs. (12) and (13) can be transformed to the following:

$$\sum_{(p_k,q_k)\in\Lambda_R} \mathscr{X}_V\,[w-p_k,\ u-q_k]\,\mathscr{A}_V\,[p_k,\ q_k] \approx \sum_{(p_k,q_k)\in\Lambda_R} \mathscr{X}_V^*[-w-p_k,\ -u-q_k]\,\mathscr{A}_V^*[p_k,\ q_k] \tag{14}$$

$$\sum_{(p_k,q_k)\in\Lambda_R} \mathscr{X}_H\,[w-p_k,\ u-q_k]\,\mathscr{A}_H\,[p_k,\ q_k] \approx \sum_{(p_k,q_k)\in\Lambda_R} \mathscr{X}_H^*[-w-p_k,\ -u-q_k]\,\mathscr{A}_H^*[p_k,\ q_k] \tag{15}$$

Since each entry in $\mathscr{X}_V$ and $\mathscr{A}_V$ is a complex number, i.e., $\mathscr{X}_V = \mathscr{X}_{Vr} + \mathrm{j}\mathscr{X}_{Vi}$ and $\mathscr{A}_V = \mathscr{A}_{Vr} + \mathrm{j}\mathscr{A}_{Vi}$, respectively, where the subscripts r and i denote the real and imaginary components of complex numbers, we can rewrite Eq. (14) as the pair of relationships below.

$$\begin{aligned}
&\sum_{(p_k,q_k)\in\Lambda_R} \mathscr{X}_{Vr}[w-p_k,\ u-q_k]\,\mathscr{A}_{Vr}[p_k,\ q_k] - \sum_{(p_k,q_k)\in\Lambda_R} \mathscr{X}_{Vi}[w-p_k,\ u-q_k]\,\mathscr{A}_{Vi}[p_k,\ q_k]\\
&- \sum_{(p_k,q_k)\in\Lambda_R} \mathscr{X}_{Vr}[-w-p_k,\ -u-q_k]\,\mathscr{A}_{Vr}[p_k,\ q_k] + \sum_{(p_k,q_k)\in\Lambda_R} \mathscr{X}_{Vi}[-w-p_k,\ -u-q_k]\,\mathscr{A}_{Vi}[p_k,\ q_k] \;\approx\; 0
\end{aligned} \tag{16}$$

$$\begin{aligned}
&\sum_{(p_k,q_k)\in\Lambda_R} \mathscr{X}_{Vr}[w-p_k,\ u-q_k]\,\mathscr{A}_{Vi}[p_k,\ q_k] + \sum_{(p_k,q_k)\in\Lambda_R} \mathscr{X}_{Vi}[w-p_k,\ u-q_k]\,\mathscr{A}_{Vr}[p_k,\ q_k]\\
&+ \sum_{(p_k,q_k)\in\Lambda_R} \mathscr{X}_{Vr}[-w-p_k,\ -u-q_k]\,\mathscr{A}_{Vi}[p_k,\ q_k] + \sum_{(p_k,q_k)\in\Lambda_R} \mathscr{X}_{Vi}[-w-p_k,\ -u-q_k]\,\mathscr{A}_{Vr}[p_k,\ q_k] \;\approx\; 0
\end{aligned} \tag{17}$$

Let $\overline{\mathscr{A}_{Vr}}$ denote the vectorized annihilating filter $\mathscr{A}_{Vr}$ in Λ_R, and let $\mathscr{H}_{r+}$ denote the chopped low rank convolution matrix composed of $\mathscr{X}_{Vr}$, i.e.

$$\mathcal{H}_{r+}(l,\ k) \;=\; \mathscr{X}_{Vr}[w_l - p_k,\ u_l - q_k]. \tag{18}$$

Then, $\sum_{(p_k,q_k)\in\Lambda_R} \mathscr{X}_{Vr}[w-p_k,\ u-q_k]\,\mathscr{A}_{Vr}[p_k,\ q_k]$ can be reformulated as a matrix-vector product: $\mathcal{H}_{r+}\overline{\mathscr{A}_{Vr}}$.

The other three 2D Hankel-like matrices $\mathscr{H}_{r-} \in \mathbb{C}^{L\times N_R}$, $\mathscr{H}_{i+} \in \mathbb{C}^{L\times N_R}$, and $\mathscr{H}_{i-} \in \mathbb{C}^{L\times N_R}$ can be constructed likewise, which respectively have elements as follows:

$$\begin{aligned}
\mathcal{H}_{r-}(l,\ k) &= \mathscr{X}_{Vr}[-w_l - p_k,\ -u_l - q_k]\ ,\\
\mathcal{H}_{i+}(l,\ k) &= \mathscr{X}_{Vi}[w_l - p_k,\ u_l - q_k]\ ,\\
\mathcal{H}_{i-}(l,\ k) &= \mathscr{X}_{Vi}[-w_l - p_k,\ -u_l - q_k]\ .
\end{aligned} \tag{19}$$

According to Eqs. (18) and (19), Eqs. (16) and (17) can be expressed as

$$\begin{bmatrix} \mathcal{H}_{r+} & -\mathcal{H}_{r-} & -\mathcal{H}_{i+} & \mathcal{H}_{i-} \\ \mathcal{H}_{i+} & \mathcal{H}_{i-} & \mathcal{H}_{r+} & \mathcal{H}_{r-} \end{bmatrix} \begin{bmatrix} \overline{\mathscr{A}_{Vr}} \\ \overline{\mathscr{A}_{Vi}} \end{bmatrix} \;\approx\; 0. \tag{20}$$

We denote $S_V \in \mathbb{C}^{2L\times 2N_R}$ as

$$S_V \;=\; \begin{bmatrix} \mathcal{H}_{r+} & -\mathcal{H}_{r-} & -\mathcal{H}_{i+} & \mathcal{H}_{i-} \\ \mathcal{H}_{i+} & \mathcal{H}_{i-} & \mathcal{H}_{r+} & \mathcal{H}_{r-} \end{bmatrix}. \tag{21}$$

Since all the entries in S_V come from $\mathscr{X}_V$, for simplicity, we use an operator $\mathscr{T}\{\cdot\}: \mathbb{C}^{m\times n} \to \mathbb{C}^{2L\times 2N_R}$ to represent this mapping, $S_V = \mathscr{T}(\mathscr{X}_V)$. Matrix S_H can be obtained in the same way, but the entries come from $\mathscr{X}_H$. From Eq. (20), we know that matrices S_V and S_H are rank-deficient.

As described above, we introduce the idea behind the LORAKS method to the gradient domain. The matrices C_V and C_H have the same structure as C but their entries are weighted k-space data. The matrices S_V and S_H have the same structure as S but consist of weighted k-space data.

2.2. Recovery of X_V and X_H

Since T_V and T_H are rank deficient, X_V and X_H can be recovered by enforcing the low rankness of T_V and T_H, and the image can be reconstructed via the least squares (LS) method. The overview of our method is shown in Fig. 2. In this section, the low rank matrix based method (LR) for recovering X_V and X_H will be described in detail.

Given the undersampled k-space data y, the undersampled Fourier transform data of the difference images y_V and y_H can be obtained by Eq. (22) as follows:

$$\begin{aligned}
y_V(w,\ u) &= (1 - e^{-2\pi \mathrm{j}w/m})y(w,\ u)\\
y_H(w,\ u) &= (1 - e^{-2\pi \mathrm{j}u/n})y(w,\ u)
\end{aligned} \tag{22}$$

Matrices X_V and X_H can be recovered by solving the following optimization problem, respectively:

$$\widehat{X}_V = \underset{X_V}{\operatorname{argmin}}\ \frac{1}{2}\|\mathscr{S}\mathcal{F}X_V - y_V\|_F^2 + \lambda\,\|\mathscr{T}\{\mathcal{F}X_V\}\|_* \tag{23}$$

$$\widehat{X}_H = \underset{X_H}{\operatorname{argmin}}\ \frac{1}{2}\|\mathscr{S}\mathcal{F}X_H - y_H\|_F^2 + \lambda\,\|\mathscr{T}\{\mathcal{F}X_H\}\|_* \tag{24}$$

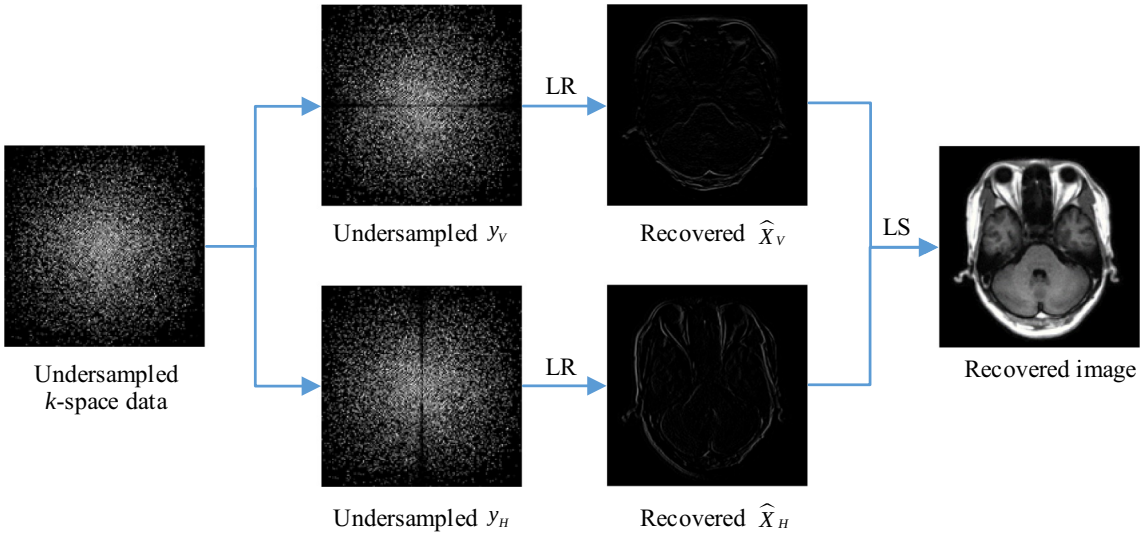

Fig. 2. Overview of our two-step method. First, we recover the vertical and horizontal difference images $\widehat{X}_V$ and $\widehat{X}_H$ from the undersampled weighted *k*-space data y_V and y_H respectively. Then the image X is recovered using the least squares (LS) method.

Table 1
Algorithm for solving Eq. (23).

Input: estimated rank r, filter radius R, parameter λ, ρ, maximum number of iteration $k_{\max}$, convergence condition η_{tol}.

Calculate y_V by Eq. (18); **SVD**: $\mathcal{T}\{y_V\} \approx U_1 \Sigma U_2^H$, where $U_1 \in \mathbb{C}^{2L\times r}$, $\Sigma \in \mathbb{C}^{r\times r}$, and $U_2 \in \mathbb{C}^{2N_R\times r}$.

Initialize $M^{(0)}=U_1\Sigma$, $N^{(0)}=U_2$, $\theta^{(0)}$, $X_V^{(0)}=\mathcal{F}^{-1}y_V$.

For $k = 1, 2, \ldots,$ *until* $(k > k_{\max})$ *or* $(\eta_k \le \eta_{tol})$

a) Solve Eq. (28) for $X_V^{(k)}$

b) Solve Eq. (29) for $M^{(k)}$

c) Solve Eq. (30) for $N^{(k)}$

d) Update $\theta^{(k)}$ by Eq. (31)

e) Compute $\eta^{(k)} = \dfrac{\left\|X_V^{(k)} - X_V^{(k-1)}\right\|}{\left\|X_V^{(k-1)}\right\|}$

End

Output: The recovered difference image $\widehat{X}_V$.

Table 2
Proposed method. First, we recover the vertical and horizontal difference images $\widehat{X}_V$ and $\widehat{X}_H$ from the undersampled weighted *k*-space y_V, y_H by the algorithm summarized in Table 1 respectively, and then the image $\widehat{\mathcal{X}}$ can be estimated using the least squares (LS) method.

Input: undersampled *k*-space data y, estimated rank r, filter radius R, parameter λ, ρ, maximum number of iteration $k_{\max}$, convergence condition η_{tol}.

Calculate y_V and y_H by Eq. (22).

Initialize $M_V^{(0)}$, $N_V^{(0)}$, $\theta_V^{(0)}$, $M_H^{(0)}$, $N_H^{(0)}$, $\theta_H^{(0)}$, $X_V^{(0)}=y_V$ and $X_H^{(0)}=y_H$.

1) Parallel calculation.

Estimate $\widehat{X}_V$ by the algorithm as shown in Table 1.	Estimate $\widehat{X}_H$ by the algorithm as shown in Table 1.

2) Without noise: solve model Eq.(32) for $\widehat{\mathcal{X}}$ by Eq.(34); under noise: solve Eq.(33).

Output: The reconstructed image $\widehat{X} = \mathcal{F}^{-1}\widehat{\mathcal{X}}$.

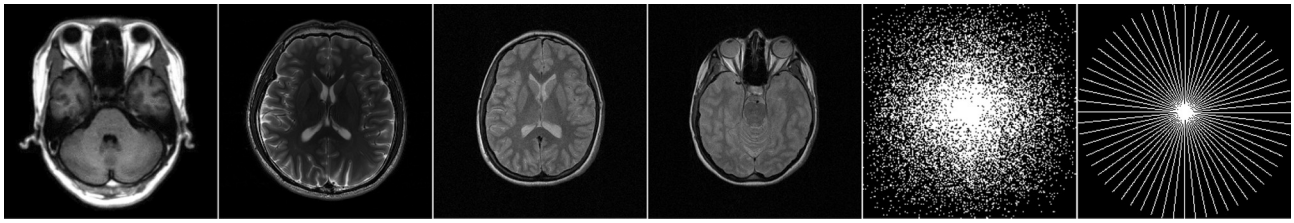

(a) Image1 (b) Image2 (c) Image3 (d) Image4 (e) Mask1 (f) Mask2

Fig. 3. (a–d) gold standard images used in the experiment; (e) variable density random mask; (f) pseudo radial sampling mask.

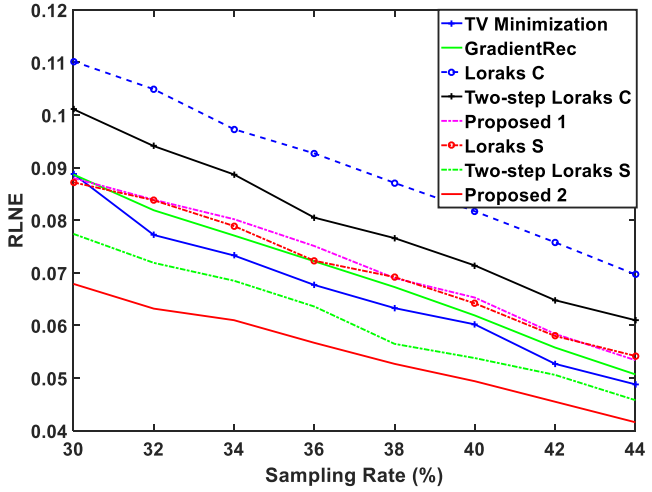

Fig. 4. RLNE curves of the eight methods for reconstructing Image2 under different sampling rates. The variable density random mask is used for simulation.

where $\mathscr{S}$ is a random undersampled sampling matrix composed of 0 and 1 entries, $\mathscr{F}$ corresponds to the Fourier transform operator, and λ is the regularization parameter. The first term in Eqs. (23) and (24) guarantees data consistency. The second term enhances the low rankness of T_V or T_H. The nuclear norm of T_V or T_H is the sum of the singular values of T_V or T_H, respectively. Many algorithms [26–29] have been successfully proposed to minimize nuclear norms, but most of them use SVD, which is time consuming, which becomes increasingly expensive as the sizes and ranks of the underlying matrices increase. In this paper, the nuclear norm of the matrix is replaced by the minimum Frobenius norm of the two factorization matrices, as shown in Eq. (25), which reduces the computational times due to SVD [30–32]:

$$\| T_V \|_* = \min_{M,\ N} \frac{1}{2}(\|M\|_F^2 + \|N\|_F^2)\ s.\ t.\quad MN^H = T_V \tag{25}$$

where the superscript H stands for the Hermitian transpose. Obviously, the low-rank matrix T_V with a size of $m \times n$ can be expressed, non-uniquely, as a matrix product $T_V = M_{m\times r} N_{n\times r}{}^H$. The initial M and N can be determined by solving the following optimization problem using the LMaFit method [33–34],

$$\min_{M,\ N,\ T_V} \frac{1}{2} \| MN^H - T_V \|_F^2 \quad s.\ t. \quad T_V(i,j) = Q(i,j)\ ,\ \ \forall\ (i,j) \in \Omega,$$

where Q consists of undersampled weighted k-space data, and the index set Ω denotes the supports of the known elements in T_V. Another way to determine the initial M and N is as follows: $M^{(0)} = US$, $N^{(0)} = V$, where $U_{m\times r} S_{r\times r} V_{n\times r}{}^H \approx SVD(Q)$, and r is a parameter to be adjusted.

According to Eq. (25), the problem in Eq. (23) can be reformulated as

$$(\widehat{X}_V, \widehat{M}, \widehat{N}) = \arg\min_{X_V,M,N} \frac{1}{2}\| \mathscr{S}\mathscr{F}X_V - y_V \|_F^2 + \frac{\lambda}{2}(\|M\|_F^2 + \|N\|_F^2)\ s.\ t.\ MN^H = \mathscr{T}\{\mathscr{F}X_V\} \tag{26}$$

where $\widehat{X}_V$ is the estimator of X_V, $\widehat{M}$ is the estimator of M, and $\widehat{N}$ is the estimator of N. The associated Lagrangian function of the alternating direction method of multipliers (ADMM) is given by

$$L(X_V, M, N, \theta) = \frac{1}{2}\| \mathscr{S}\mathscr{F}X_V - y_V \|_F^2 + \frac{\lambda}{2}(\|M\|_F^2 + \|N\|_F^2) + \frac{\lambda\rho}{2}\| \mathscr{T}\{\mathscr{F}X_V\} - MN^H + \theta\|_F^2. \tag{27}$$

Then, each subproblem is obtained as follows.

$$X_V^{(k)} = \operatorname*{argmin}_{X_V} \frac{1}{2}\| \mathscr{S}\mathscr{F}X_V - y_V \|_F^2 + \frac{\lambda\rho}{2}\| \mathscr{T}\{\mathscr{F}X_V\} - M^{(k-1)}N^{(k-1)H} + \theta^{(k-1)} \|_F^2 \tag{28}$$

$$M^{(k)} = \operatorname*{argmin}_{M} \frac{\lambda}{2}\|M\|_F^2 + \frac{\lambda\rho}{2}\| \mathscr{T}\{\mathscr{F}X_V^{(k)}\} - MN^{(k-1)H} + \theta^{(k-1)} \|_2^2 \tag{29}$$

$$N^{(k)} = \operatorname*{argmin}_{N} \frac{\lambda}{2}\|N\|_F^2 + \frac{\lambda\rho}{2}\| \mathscr{T}\{\mathscr{F}X_V^{(k)}\} - M^{(k)}N^H + \theta^{(k-1)} \|_2^2 \tag{30}$$

$$\theta^{(k)} = \mathscr{T}\{\mathscr{F}X_V^{(k)}\} - M^{(k)}N^{(k)H} + \theta^{(k-1)} \tag{31}$$

The algorithm we used to solve Eq. (23) is summarized in Table 1. Similarly, $\widehat{X}_H$ can be obtained with the same method.

2.3. Image reconstruction

After we obtain $\widehat{X}_V$, $\widehat{X}_H$, we will solve the following optimization problem to recover the image X.

$$\begin{aligned} \widehat{\mathscr{X}} &= \operatorname*{argmin}_{\mathscr{X}} \|\mathscr{X}_V - \widehat{\mathscr{X}_V}\|_F^2 + \|\mathscr{X}_H - \widehat{\mathscr{X}_H}\|_F^2 + \gamma\ \|\mathscr{S}\mathscr{X} - y\|_F^2 \\ \widehat{X} &= \mathscr{F}^{-1}\widehat{\mathscr{X}} \end{aligned} \tag{32}$$

where $\mathscr{F}^{-1}$ denotes the inverse Fourier transform operator, $\widehat{\mathscr{X}_V} = \mathscr{F}\widehat{X}_V$, $\widehat{\mathscr{X}_H} = \mathscr{F}\widehat{X}_H$, $\mathscr{X}_V = (1 - e^{-2\pi \mathrm{j} w/m})\mathscr{X}$, $\mathscr{X}_H = (1 - e^{-2\pi \mathrm{j} u/n})\mathscr{X}$. We can obtain $\widehat{\mathscr{X}}$ via the least squares (LS) method:

$$\widehat{\mathscr{X}}(w,\ u) = \frac{(1 - e^{2\pi \mathrm{j} w/m})\widehat{\mathscr{X}_V}(w,\ u) + (1 - e^{2\pi \mathrm{j} u/n})\widehat{\mathscr{X}_H}(w,\ u) + \gamma y}{(|1 - e^{-2\pi \mathrm{j} w/m}|^2 + |1 - e^{-2\pi \mathrm{j} u/n}|^2) + \gamma I_{\Omega_{\mathscr{S}}}} \tag{33}$$

where $\Omega_{\mathscr{S}}$ is the position set of element 1 in $\mathscr{S}$. Finally, our method is summarized in Table 2. In the presence of noise, parameter γ is empirically chosen as 0.1. Without noise, we can obtain $\widehat{\mathscr{X}}$ via Eq. (34).

$$\widehat{\mathscr{X}}(w,\ u) = \begin{cases} \dfrac{(1 - e^{2\pi \mathrm{j} w/m})\widehat{\mathscr{X}_V}(w,\ u) + (1 - e^{2\pi \mathrm{j} u/n})\widehat{\mathscr{X}_H}(w,\ u)}{|1 - e^{-2\pi \mathrm{j} w/m}|^2 + |1 - e^{-2\pi \mathrm{j} u/n}|^2}, & (w,\ u) \notin \Omega_{\mathscr{S}} \\ y(w,\ u), & (w,\ u) \in \Omega_{\mathscr{S}} \end{cases} \tag{34}$$

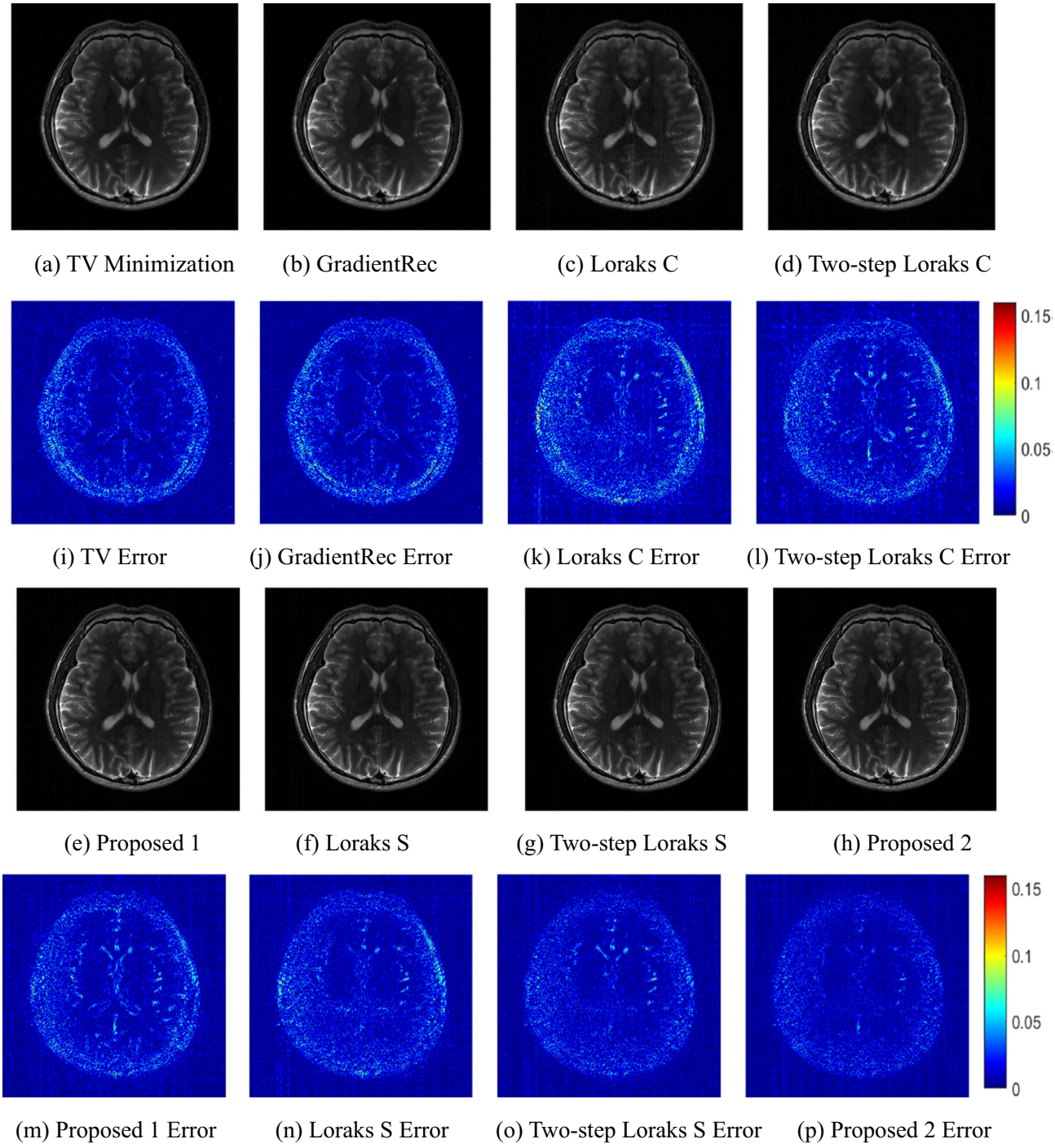

Fig. 5. The magnitude images (the first and the third row) and error images (the second and the fourth row), SR = 30%, variable density random sampling mask. (a) TV Minimization reconstruction, RLNE = 8.67%. (b) GradientRec reconstruction, RLNE = 8.85%. (c) Loraks C reconstruction with r_C = 30, RLNE = 11.04%. (d) Two-step Loraks C reconstruction with r_C = 26, RLNE = 9.84%. (e) Proposed 1, RLNE = 8.76%. (f) Loraks S reconstruction with r_S = 30, RLNE = 8.74%. (g) Two-step Loraks S reconstruction with r_S = 30, RLNE = 7.62%. (h) Proposed 2, RLNE = 6.71%. (i)–(p) Error images corresponding to the magnitude images shown in (a)–(h). Images (a)–(i) have been normalized such that the greyscales range from 0 to 1.

The above two schemes are relatively simple, but they are effective. Other more complicated schemes for reconstructing the image X from X_V and X_H can be found in references [24,35].

3. Experimental results

The objective of this section is to demonstrate the potential of our methods in a variety of settings and to compare with other CS-MRI methods. All simulations were carried out on Windows 10 and MATLAB R2016a running on a PC with an Intel Core i5 CPU 3.2 GHz with 12 GB of memory. Data acquisition was simulated by undersampling the 2D discrete Fourier transform of the MR images. The number of measurements is quantified in terms of the percentage of fully sampled Fourier coefficients, referred to as the sampling rate (SR). For quantitative evaluation, the reconstruction quality was measured by the relative least normalized error (RLNE) which is a standard image quality metric indicating the difference between the reconstruction $\widehat{X}$ and the gold standard image X:

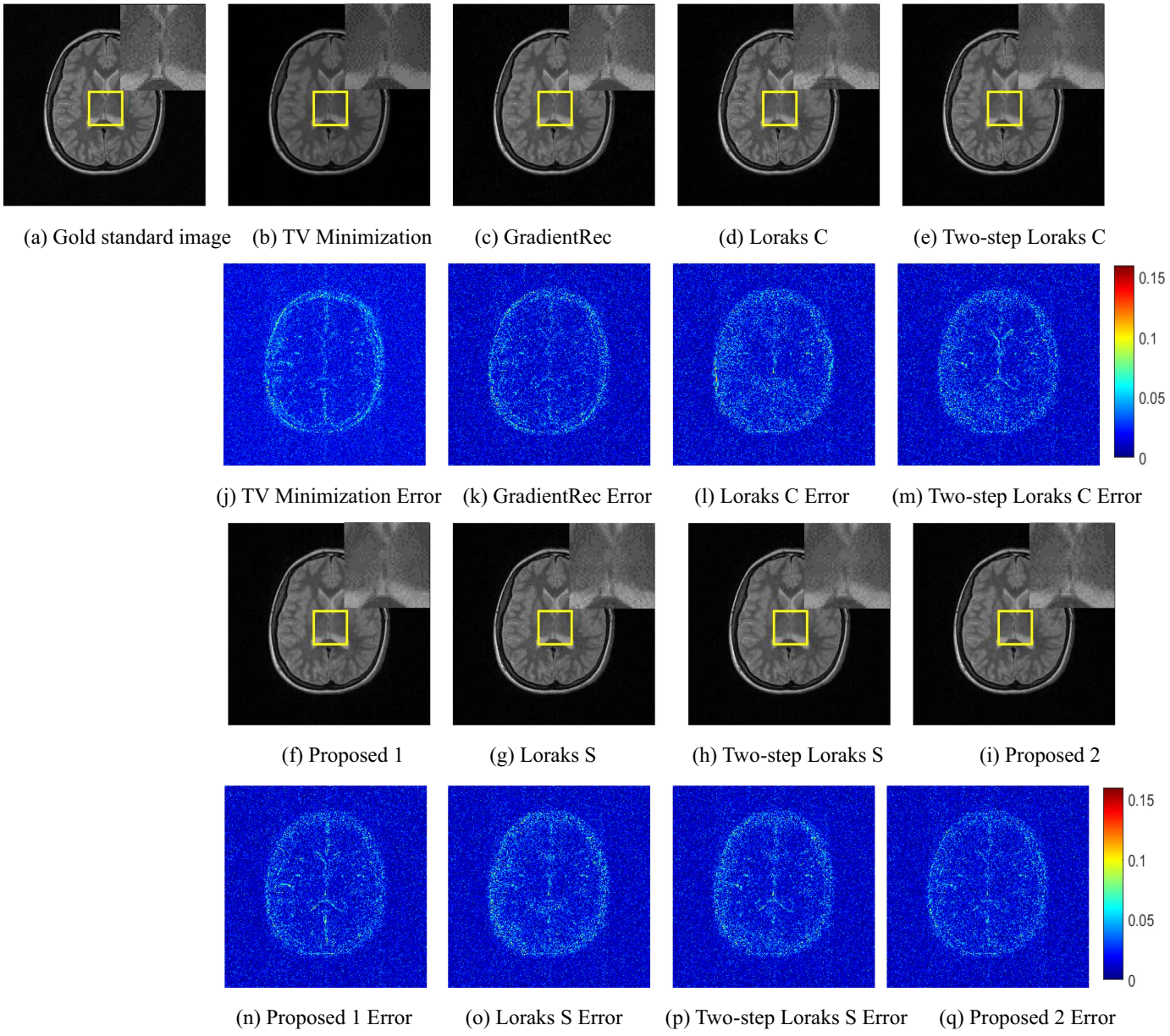

Fig. 6. The magnitude images (the first and the third row) and the error images (the second and the fourth rows), SR = 30%, variable density random sampling mask. (a) Gold standard image. (b) TV Minimization reconstruction, RLNE = 10.54%. (c) GradientRec reconstruction, RLNE = 9.29%. (d) Loraks C reconstruction with r_C = 25, RLNE = 9.78%. (e) Two-step Loraks C reconstruction with r_C = 19, RLNE = 9.40%. (f) Proposed 1, RLNE = 9.08%. (g) Loraks S reconstruction with r_S = 25, RLNE = 9.48%. (h) Two-step Loraks S reconstruction with r_S = 19, RLNE = 9.16%. (i) Proposed 2, RLNE = 8.84%. (j)–(q) Error images corresponding to the magnitude images shown in (a)–(h). Images (a)–(i) have been normalized such that the greyscales range from 0 to 1.

$$\zeta_{RLNE} = \frac{\|\widehat{X} - X\|_F}{\|X\|_F}$$

3.1. Comparisons in sparse sampling examples

The experiments were conducted on both real-valued images and complex-valued images. The real-valued Image1 shown in Fig. 3(a) came from a fully sampled proton density weighted image acquired from the 0.35 T scanner. The complex-valued Image2 of size 256 × 256 in Fig. 3(b) [36] was acquired from a healthy volunteer at a 3 T Siemens Trio Tim MRI scanner using the T2-weighted turbo spin echo sequence (TR/TE = 6100/99 ms, 220 × 220 mm field of view, 3 mm slice thickness). The complex-valued Image3 and Image4 in Fig. 3(c–d) were extracted from the in vivo dataset from [37]. This dataset contains 38 slices with 256 × 256 resolution, using a TSE sequence (1 × 1 mm in-plane spatial resolution with 3 mm thick contiguous slices, TR = 6000 ms, TE = 27 ms). The variable density sampling and pseudo radial sampling are adopted as shown in Fig. 3(e), (f).

For simplicity, our proposed reconstruction scheme using C_V and C_H is named Proposed 1, and our proposed reconstruction scheme using S_V and S_H is named Proposed 2. To "fairly" compare the performance of the proposed low-rank method, in addition to the traditional CS-MRI methods, we also conduct experiments with the MM algorithm used in LORAKS to reconstruct the gradient image, and then recover the image. We call this method "Two-step LORAKS"; Two-step Loraks C stands for the "Two-step LORAKS" method using matrix C and Two-step Loraks S is the method using matrix S. Thus, the reconstruction methods we compared here are: (1) the TV Minimization method [9], (2) the GradientRec method [24], (3) the matrix Cbased LORAKS method (Loraks C) [20], (4) the matrix S based LORAKS method (Loraks S) [20], (5) Two-step Loraks

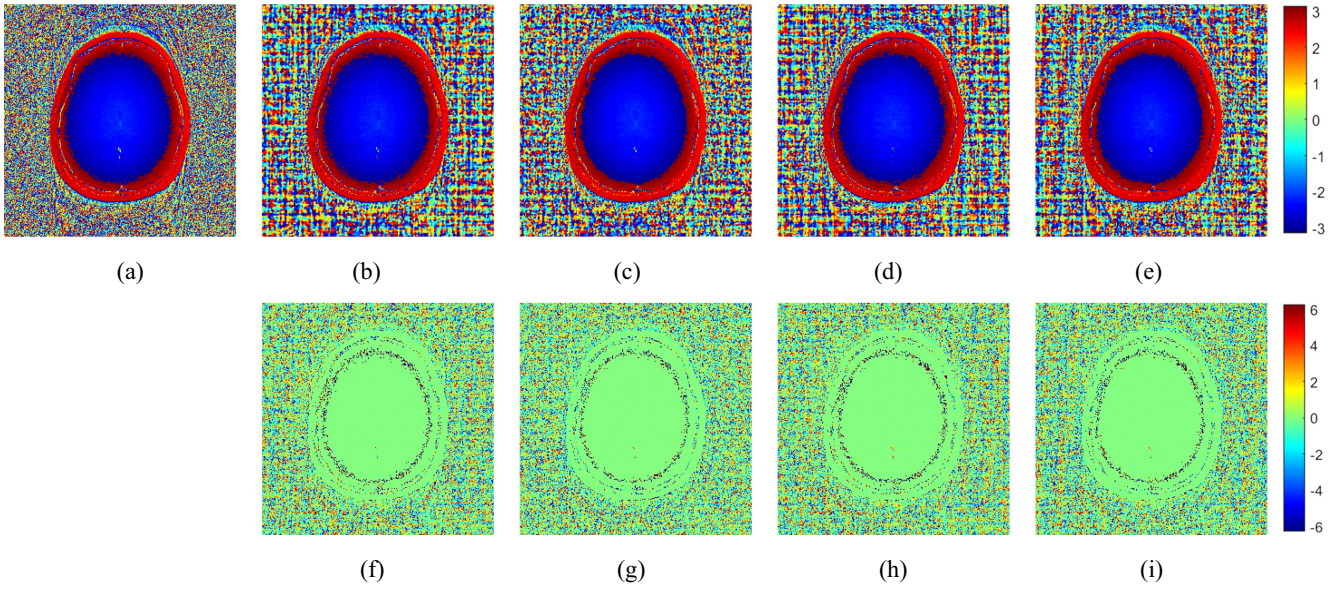

Fig. 7. The phase images and error images (image3). (a) Original, (b) Loraks C, (c) Loraks S, (d) Proposed 1, (e) Proposed 2, (f)–(i) Error images corresponding to the phase images shown in (a)–(e). The results reconstructed from 30% of the variable density random sampling data.

Table 3
RLNEs of the eight methods with the variable density random sampling mask.

Data	Methods	RLNE (%)	
		SR = 30%	SR = 40%
Image1	TV Minimization	3.86	2.70
	GradientRec	3.53	2.55
	Loraks C	5.28	3.66
	Two-step Loraks C	4.79	3.20
	Proposed 1	4.29	3.05
	Loraks S	3.48	2.89
	Two-step Loraks S	3.24	2.50
	Proposed 2	3.13	2.41
Image4	TV minimization	8.89	7.69
	GradientRec	9.08	7.83
	Loraks C	9.32	8.14
	Two-step Loraks C	9.12	7.78
	Proposed 1	8.98	7.92
	Loraks S	9.19	7.92
	Two-step Loraks S	9.05	7.75
	Proposed 2	8.72	7.67

Table 4
RLNEs of the eight methods with the pseudo radial sampling mask.

Data	Methods	RLNE (%)	
		SR = 30%	SR = 40%
Image1	TV Minimization	3.61	2.76
	GradientRec	3.52	2.74
	Loraks C	4.53	3.10
	Two-step Loraks C	4.19	2.77
	Proposed 1	3.87	2.68
	Loraks S	3.16	2.22
	Two-step Loraks S	2.91	2.15
	Proposed 2	2.85	2.11
Image4	TV Minimization	9.90	7.64
	GradientRec	8.96	7.84
	Loraks C	9.41	8.03
	Two-step Loraks C	8.98	7.58
	Proposed 1	8.70	7.44
	Loraks S	9.05	7.53
	Two-step Loraks S	8.67	7.41
	Proposed 2	8.59	7.36

Table 5
Runtime of the six low-rank matrices methods for reconstructing image1 and image4.

Methods	Runtime (s)	
	Image1	Image4
Loraks C	130.66	167.49
Two-step Loraks C	292.16	231.17
Proposed 1	77.87	80.28
Loraks S	224.40	180.39
Two-step Loraks S	478.54	306.52
Proposed 2	152.03	242.93

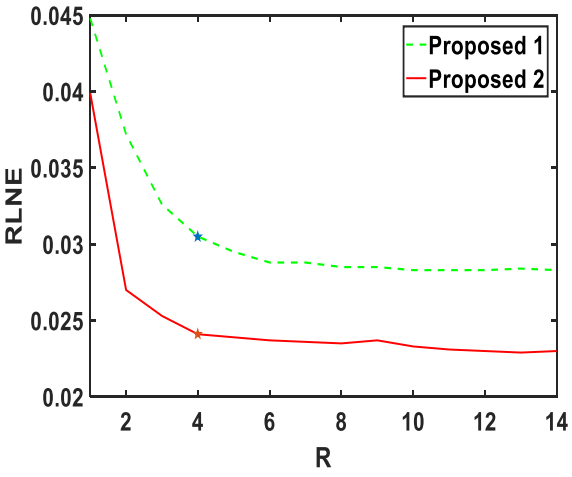

Fig. 8. RLNE values versus the filter radius R for the reconstruction of image1 under variable density random mask (SR = 40%). Asterisks indicate the selected R-values.

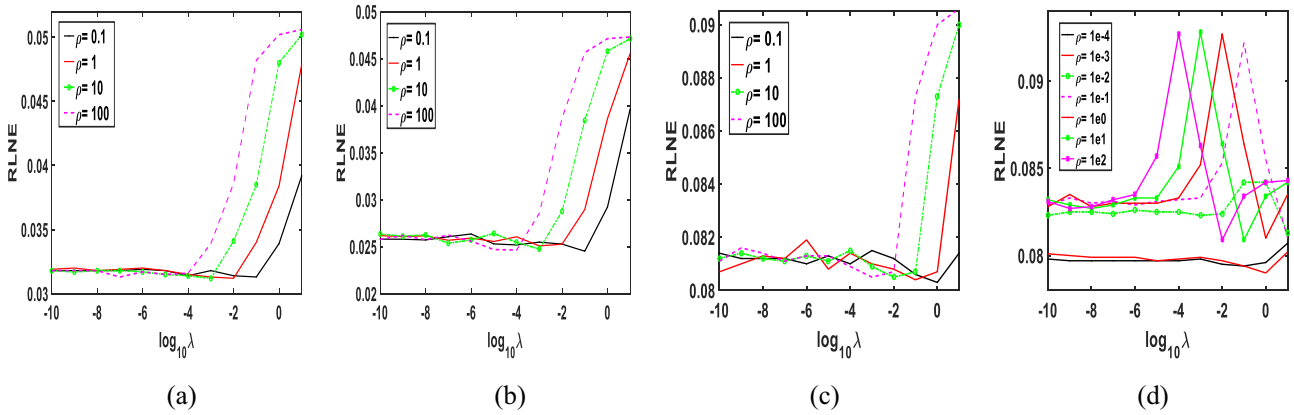

Fig. 9. RLNEs versus parameters λ and ρ for the reconstruction of real-valued Image1 and complex-valued Image3 under variable density sampling (SR = 40%): (a) Proposed 1, Image1; (b) Proposed 2, Image1; (c) Proposed 1, Image3; (d) Proposed 2, Image3.

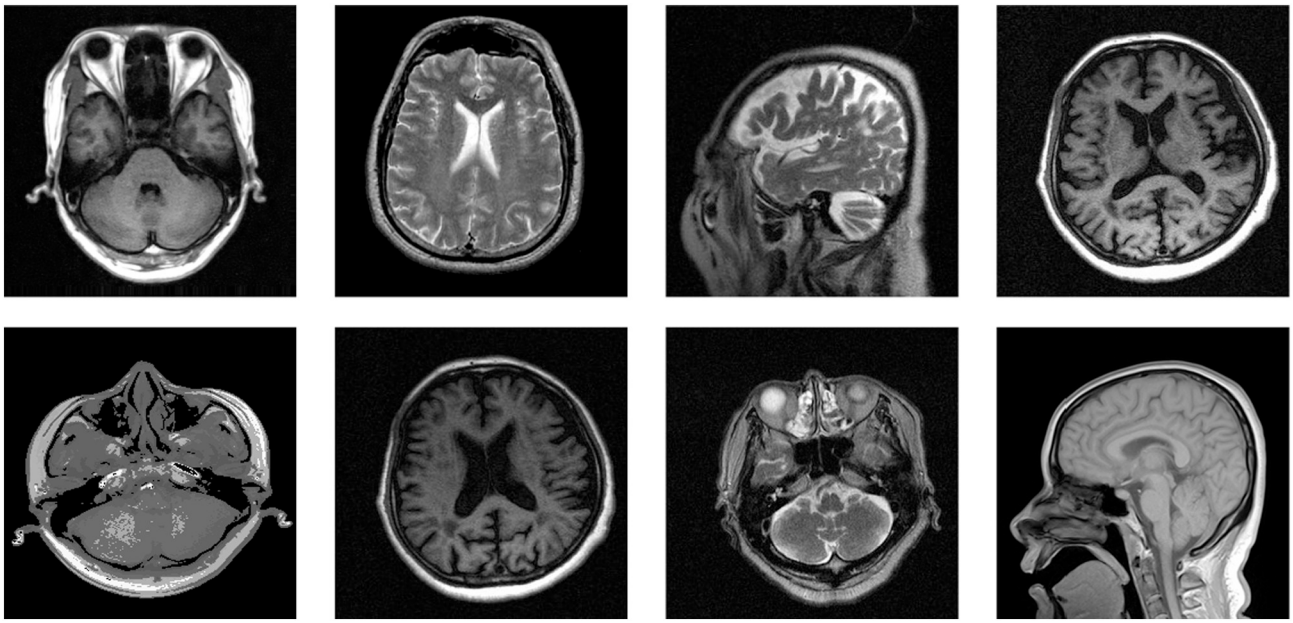

Fig. 10. Images (256 × 256) used to show the stability of parameter λ selection in Fig. 11. Image1–8 are from left to right and from top to bottom.

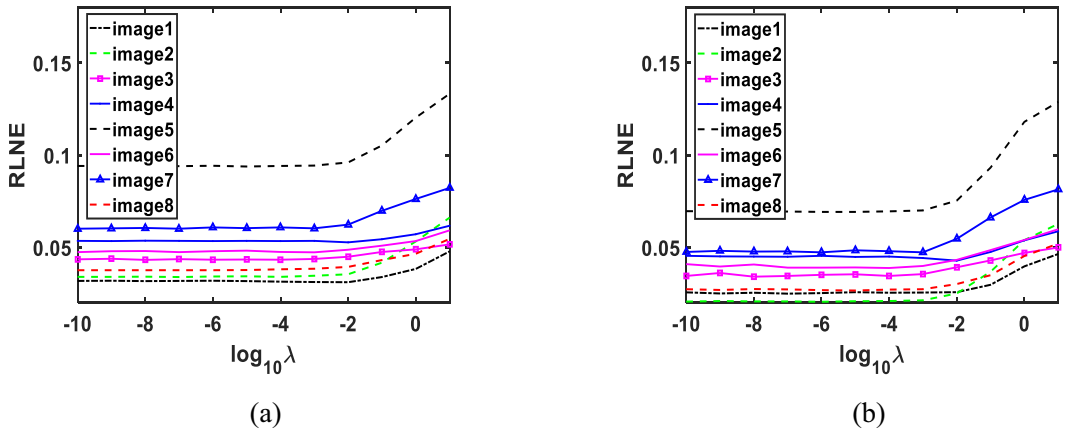

Fig. 11. RLNEs versus λ for the reconstruction of different images with ρ = 1 under variable density sampling (SR = 40%). (a) Proposed 1, (b) Proposed 2.

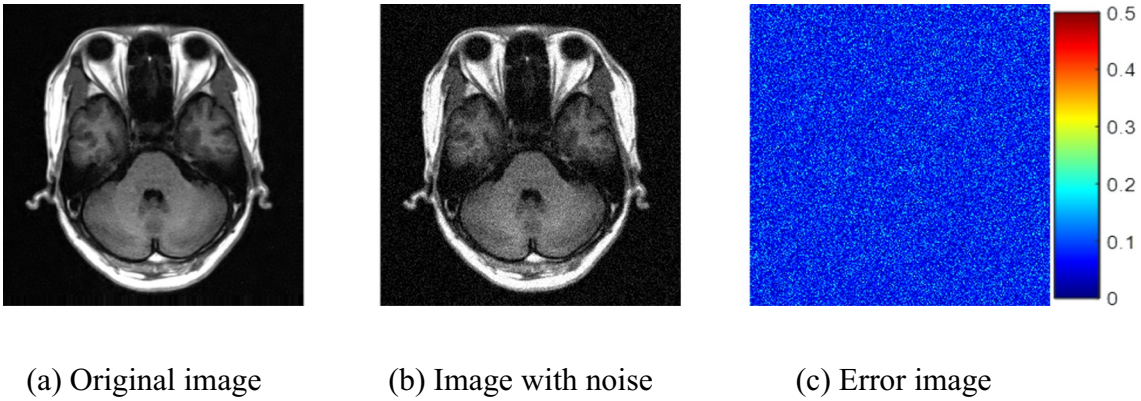

Fig. 12. The original image and noisy images. (a) Original image. (b) Image with noise, RLNE = 17.63%. (c) Error mage.

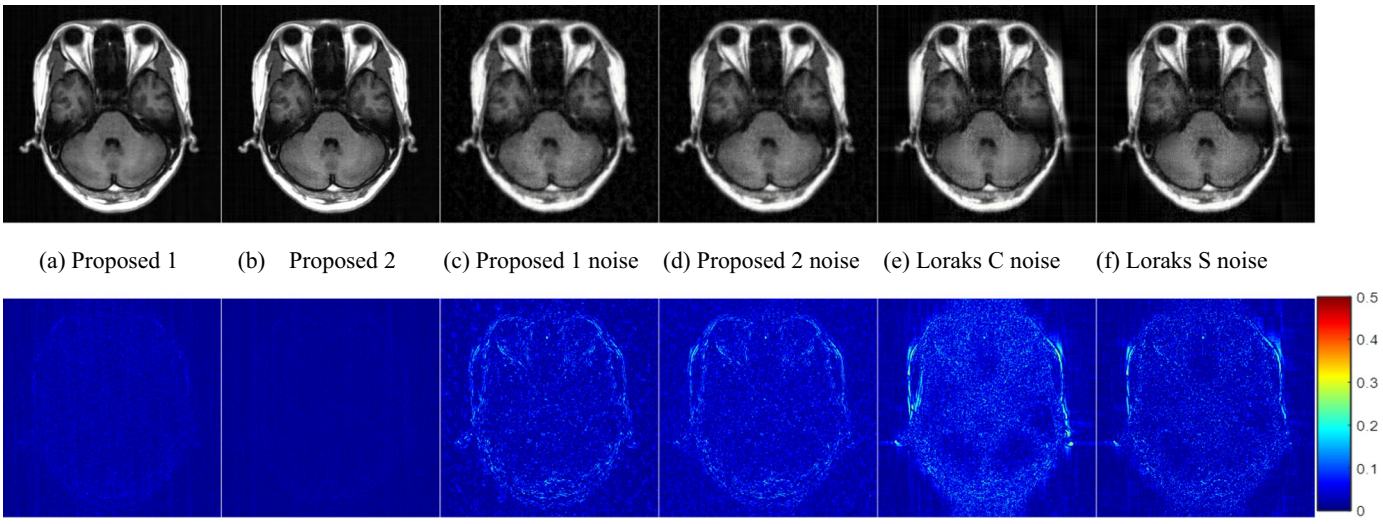

Fig. 13. The reconstructed images (first row) and error images (second row), SR = 30%, variable density random sampling mask, $R = 4$. (a) Proposed 1 method without noise, RLNE = 4.29%; (b) Proposed 2 method without noise, RLNE = 3.13%; (c) Proposed 1 method with noise, RLNE = 11.07%; (d) Proposed 2 method with noise, RLNE = 10.39%; (e) Loraks C method with noise, RLNE = 12.83%; (f) Loraks S method with noise, RLNE = 11.7%. (g)–(l) Error images corresponding to the reconstructions shown in (a)–(f).

C, (6) Two-step Loraks S, (7) Proposed 1 and (8) Proposed 2.

To objectively compare the different methods, we run the source code for TV Minimization,[1] GradientRec,[2] Loraks C and Loraks S[3] provided by the respective authors online. In addition, the optimal parameters are used to guarantee the performance of each method. The maximum number of iterations $k_{\max} = 100$, and the convergence condition $\eta_{tol} = 10^{-5}$.

The RLNE curves of the eight methods for reconstructing the complex-valued Image2 under different sampling rates are shown in Fig. 4. We can see that the Loraks C method has the highest RLNEs and the Proposed 2 method has the lowest RLNEs under sampling rate from 30% to 44%. RLNEs of the Two-step Loraks C method are lower than those of the original Loraks C, but higher than those of Proposed 1 method. RLNEs of the Two-step Loraks S method are lower than those of the original Loraks S, but higher than those of Proposed 2 method.

The reconstruction results (the magnitude images and the error images) of Image2 using the eight methods are shown in Fig. 5. The reconstruction results of Image3 are shown in Figs. 6 and 7, where the magnitude and error images are in Fig. 6, the phase images and error images are in Fig. 7. We can see that two-step Loraks methods outperforms corrresponding original Loraks methods, but they have slightly blurred image details compared with the Proposed 2 method, as shown in the yellow block in Fig. 6. Over-smoothing and block effects exist in the results of TV Minimization method. From Fig. 7 we can see that our methods can maintain the phase information when reconstructing the complex image.

RLNEs under different sampling rates and different sampling masks are summarized in Tables 3 and 4. The results also demonstrate that the Proposed 2 method outperforms the other methods.

Since our methods need to solve two optimization problems, the computational time is a concern. Fortunately, we chose ADMM algorithm and an SVD-free scheme to fulfil nuclear norm minimization. The running time of our method is shorter than that of LORAKS. From Table 5, we can see that Proposed 2 has running time comparable to that of Loraks C. Although Loraks C method consumes less time due to the smaller size of C, it has the worst reconstruction results. The Two-step LORAKS is more time consuming than the original LORAKS method and our methods.

[1] http://www.mlustig.com.
[2] http://www.cs.ubc.ca/labs/scl/spgl1.
[3] http://mr.usc.edu/.

3.2. Parameter evaluation

Our method involves several parameters. In this section, we conduct experiments to test how the parameters affect the reconstruction results. Fig. 8 shows how the RLNE changes as the filter radius R increases. The testing image is image1, and variable density sampling (SR = 40%) is adopted. We can see that the RLNE tends to be stable as R reaches a certain value. From [14], we know that R must be large enough to ensure that the number of columns of the low rank Hankel matrix are greater than the sparsity of the image. If R is greater than a certain value, the rank of the matrix will not change, so a low rankness constraint on the matrix will lead to the same reconstruction result. This explains why RLNE curve is shown in Fig. 8. The experiments in Section 3.1 are conducted at $R = 4$ to guarantee accuracy and rapid reconstruction.

The regularization parameters λ trade off the contribution of the data consistency term and the nuclear norm term. The parameter ρ affects the convergence of the iteration. Fig. 9 displays the plots of the RLNEs as a function of λ with ρ = 0.1–100 for real-valued image1 and complex-valued Image3. We can see that the RLNE varies slightly if λ is in the range of 10^{-10} to 10^{-4}. We also conduct the experiments on 8 MR images shown in Fig. 10 (image1–8) with ρ = 1 under variable density sampling. The results are depicted in Fig. 11, and the optimal λ is in the range of 10^{-10} to 10^{-4}. If the parameter λ is smaller than 10^{-10}, the reconstructed image will have a large error, and when λ is smaller than 10^{-15}, the image cannot be reconstructed.

3.3. Experimental results under noisy condition

To evaluate the performance of our method, we conduct experiments on noisy *k*-space data and analyse how noise affects the reconstruction results. Additive thermal noise in *k*-space data is simulated using complex Gaussian pseudo-random noise. The reconstruction results we show here are obtained via Proposed 1, Proposed 2 and LORAKS methods under noise conditions with a mean of 0 and a deviation of 15. The original image, noisy image, reconstructed results of the four methods and the corresponding error images are shown in Figs. 12 and 13. Since the *k*-space data is polluted with noise, the reconstructed images of our methods and LORAKS are degraded. From these results, we can see that our methods have results comparable to LORAKS under noisy conditions.

4. Conclusion

In this paper, we proposed a new idea to enrich the low rank matrix based CS-MR image reconstruction method. We built two matrices T_V and T_H using the weighted *k*-space according to the annihilating filter and the properties of the 2D Fourier transform. Due to the sparsity of the vertical and horizontal differences of an MR image, the matrices T_V and T_H are low rank. First, we enforced the low rankness of the matrices T_V and T_H to recover the vertical and horizontal differences. Afterwards, the image was reconstructed from these difference images via the least squares method. The final reconstruction results demonstrated that our method outperforms other low rank based methods. Our method is robust to the selection of parameters and can adapt to noise.

Acknowledgments

The authors thank Professor Vivek K Goyal for sharing the complex-valued vivo dataset for the experiments in this article. The authors also thank all the authors for providing their codes and dataset online, which helped us a lot in the experiments.

References

[1] Liang ZP. Spatiotemporal imaging with partially separable functions. Proceedings of IEEE international symposium on biomedical imaging. 2007. p. 988–91.
[2] Blumensath T. Sampling and reconstructing signals from a union of linear subspaces. IEEE Transactions on Information Theory 2011;57(7):4660–71.
[3] Babacan SD, Lam F, Peng X, et al. Interventional MRI with sparse sampling using union-of-subspaces. Proceedings of IEEE International Symposium on Biomedical Imaging. 2012. p. 314–7.
[4] Ravishankar S, Bresler Y. MR image reconstruction from highly undersampled *k*-space data by dictionary learning. IEEE Trans Med Imaging 2011;30(5):1028–41.
[5] Liang D, DiBella EVR, Chen RR, et al. k-t ISD: dynamic cardiac MR imaging using compressed sensing with iterative support detection. Magn Reson Med, 2012, 68(1): 41–53.
[6] Lustig M, Donoho DL, Santos JM, Pauly JM. Compressed sensing MRI. IEEE Signal Processing Magazine 2008;25(2):72–82.
[7] Chen C, Huang J. Compressive sensing MRI with wavelet tree sparsity. Neural Information Processing Systems (NIPS) 2012:1–9.
[8] Qu X, Zhang W, Guo D, Cai C, Cai S, Chen Z. Iterative thresholding compressed sensing MRI based on contourlet transform. Inverse Prob Sci Eng 2010;18(6):737–58.
[9] Lustig M, Donoho D, Pauly J. Sparse MRI: the application of compressed sensing for rapid MR imaging. Magn Reson Med 2007;58:1182–95.
[10] Knoll F, Bredies K, Pock T, et al. Second order total generalized variation (TGV) for MRI. Magn Reson Med, 2011, 65(2): 480–491.
[11] Liang D, Wang H, Chang Y, et al. Sensitivity encoding reconstruction with nonlocal total variation regularization. Magn Reson Med, 2011, 65(5): 1384–1392.
[12] Huang J, Zhang S, Metaxas D. Efficient MR image reconstruction for compressed MR imaging. Med Image Anal 2011;15(5):670.
[13] Chen Yuxin, Chi Yuejie. Robust spectral compressed sensing via structured matrix completion. IEEE Transaction on Information Theory 2014;60(10):6576–601.
[14] Ye JC, Kim JM, Jin Kyong Hwan, et al. Compressive sampling using annihilating filter-based low-rank interpolation. IEEE Transactions on Information Theory 2015;63(2):777–801.
[15] Candes EJ, Recht B. Exact matrix completion via convex optimization. Foundation of Computational Math 2009;9:717–72.
[16] Candes EJ, Tao T. The power of convex relaxation: near-optimal matrix completion. IEEE Trans Inf Theory 2010;56(5):2053–80.
[17] Jin Kyong Hwan, Lee Dongwook, Ye Jong Chul. A general framework for compressed sensing and parallel MRI using annihilating filter based low-rank Hankel matrix. IEEE Transactions on Computational Imaging 2016;2(4):480–95.
[18] Vetterli M, Marziliano P, Blu T. Sampling signals with finite rate of innovation. IEEE transactions on Signal Processing 2002;50(6):1417–28.
[19] Ongie G, Jacob M. Off-the-grid recovery of piecewise constant images from few Fourier samples. SIAM J Imag Sci 2016;9(3):1004–41.
[20] Haldar Justin P. Low-rank modeling of local-space neighborhoods (LORAKS) for constrained MRI. IEEE Transaction on medical imaging 2014;33(3):668–80.
[21] Haldar Justin P. Low-rank modeling of local k-space neighborhoods (LORAKS): Implementation and examples for reproducible research Technical Report USC-SIPI-414 Los Angeles, CA: University of Southern California; April 2014.
[22] Haldar Justin P, Zhuo J. P-LORAKS: low-rank modeling of local k-space neighborhoods with parallel imaging data. Magn Reson Med 2016;75(4):1499–514.
[23] Kim TH, Setsompop K, Haldar Justin P. LORAKS makes better SENSE: phase-constrained partial fourier SENSE reconstruction without phase calibration. Magn Reson Med 2017;77:1021–35.
[24] Patel Vishal M, Maleh Ray, Gilbert Anna C, Chellappa Rama. Gradient-based image recovery methods from incomplete fourier measurements. IEEE Trans Image Process 2012;21(1):94–105.
[25] Jin Kyong Hwan, Ye JC. Annihilating filter-based low-rank Hankel matrix approach for image inpainting. IEEE Trans Image Process 2015;24(11):3498–511.
[26] Yang J, Yuan X. An inexact alternating direction method for trace norm regularized least squares problem tech. rep. Dept. of Mathematics, Nanjing University; 2010.
[27] Goldfarb D, Ma S, Wen Z. Solving low rank matrix completion problems efficiently tech. rep. Invited paper at the 47th Allerton Conference on Communication, Control and Computing, Illinois2009.
[28] Cai J F, Cand, S, E J, et al. A singular value thresholding algorithm for matrix completion. Siam Journal on Optimization, 2008, 20(4):1956–1982.
[29] Peng Y, Suo J, Dai Q, et al. Reweighted low-rank matrix recovery and its application in image restoration. IEEE Transactions on Cybernetics, 2014, 44(12):2418–2430.
[30] Signoretto M, Cevher V, Suykens JA. An SVD-free approach to a class of structured low rank matrix optimization problems with application to system identification. IEEE Conf. on Decision and Control. 2013. no. EPFL-CONF-184990.
[31] N. Srebro. Learning with matrix factorizations. Ph.D. dissertation, Dept. Elect. Eng. Comput. Sci., Massachusetts Inst. Technology, Cambridge, MA, USA, 2004.
[32] Recht B, Fazel M, Parrilo PA. Guaranteed minimum-rank solutions of linear matrix equations via nuclear norm minimization. SIAM review 2010;52(3):471–501.
[33] Wen Z, Yin W, Zhang Y. Solving a low-rank factorization model for matrix completion by a nonlinear successive over-relaxation algorithm. Math Prog Comp 2012;4(4):333–61.
[34] Jin Kyong Hwan, Ye JC. Sparse and low-rank decomposition of a Hankel structured

matrix for impulse noise remova. IEEE Trans Image Process 2018;27(3):1448–61.
[35] Ravazzi C, Coluccia G, Magli E. Curl-constrained gradient estimation for image recovery from highly incomplete spectral data. IEEE Trans Image Process 2017;26(6):2656–68.
[36] Qu Xiaobo, Hou Yingkun, Lam Fan, Guo Di, Zhong Jianhui, Chen Zhong. Magnetic resonance image reconstruction from undersampled measurements using a patch-based nonlocal operator. Med Image Anal 2014;18(6):843–56.
[37] Bilgic B, Goyal V, Adalsteinsson E. Multi-contrast reconstruction with Bayesian compressed sensing. Magn Reson Med 2011;66:1601–15.

Shuli Ma received her M.S. degree in communication engineering from the Qufu Normal University in 2016. She is currently pursuing her Ph.D. degree in the School of Information and Electronics, Beijing institute of technology, Beijing, China. Her main research interests include image inpainting, reconstruction and tensor decomposition.

Huiqian Du received her BS, Master and Dr.Eng. degrees in Electrical Engineering from Beijing Institute of Technology, Beijing, China, in 1995, 1998 and 2007 respectively. In April 1998, she joined Beijing Institute of Technology, where she is currently an associate professor. Her research interests lie in the fields of image processing, image reconstrucion, machine learning.

Wenbo Mei received the B.S. degree in Electronic Engineering and M.S. Degree in Communication and Electronic System from Beijing Institute of Technology(BIT), China, in 1982 and 1993, respectively. He is professor of School of Information and Electronics, BIT. He is also a Visiting Research Fellow at University of Central Lancashire, a Visiting Professor at University of Reading UK. His research interests include wavelet transform, time-frequency analysis, compressive sensing in signal and image processing for radar, communication system and channel, MRI, etc.